High-Order Accurate Incompressible Navier–Stokes Algorithm for Vortex-Ring Interactions with Solid Wall

Debojyoti Ghosh* and James D. Baeder†
University of Maryland, College Park, Maryland 20742

The interaction of vortical structures with a solid wall is studied numerically in this paper. The incompressible Navier–Stokes equations in their primitive variable formulation are solved on a staggered Cartesian grid using the fractional-step algorithm. The convective terms are marched in time using the Adams–Bashforth or Runge–Kutta schemes, while the viscous terms are treated implicitly using the trapezoidal scheme. An upwind reconstruction of the convective fluxes in their conservative form is proposed and compared against the nonconservative flux formulation, as differences are expected due to nonzero velocity divergence in the numerical solution. The performance of the algorithm is assessed on the convection of an isolated vortex. The algorithm is verified on benchmark incompressible flows and flows involving the convection, mutual interaction, and wall impingement of vortical structures. An attempt is made to simulate the impingement of two and multiple vortex rings against a solid wall to understand the effect of mutual interactions on the interactions with a solid wall. The effects of Reynolds number and initial separation between the rings are studied. These parameters are observed to affect the behavior of the vortical structures, thus affecting the formation and ejection of secondary vortices.

Nomenclature

a	=	vortex core radius
dt	=	time step
i, j, k	=	grid indices along x, y, z, respectively
p	=	pressure
R	=	vortex ring radius
Re	=	Reynolds number
S	=	interpolation stencil
t	=	time
U	=	vortex convection speed
$\mathbf{u}^*$	=	predicted velocity field
$\mathbf{u}^n$	=	velocity field at time level n
u_i, u_j	=	i, jth component of velocity vector
u, v, w	=	Cartesian velocity components
x, y, z	=	Cartesian space coordinates
x_c, y_c	=	vortex center coordinates
x_i, x_j	=	i, jth space coordinate
δ	=	perturbation parameter in shear layer
ν	=	coefficient of kinematic viscosity
ρ	=	thickness parameter in shear layer
ϕ	=	pseudopressure
ω	=	vorticity magnitude

I. Introduction

THE study of vortex dynamics is essential to understanding the flow in a rotorcraft wake. The tip vortices shed by the rotating blades form a helical system of vortices convecting away from the rotor plane. The flow is determined by the convection and mutual interactions of these vortical structures. In addition, the wake flow of a rotorcraft operating near the ground is determined by the inter-actions of vortices with a solid wall. The accurate modeling of vortex-dominated flows is required to understand the flow around a rotorcraft. In the present study, a high-order accurate incompressible flow solver is formulated, and the impingement of multiple vortex rings against a solid wall is studied to understand the interactions of vortical structures with the ground boundary layer.

The formation and convection of vortex rings and their mutual interactions as well as interactions with a solid wall have been studied in literature [1–3]. The flow physics behind the impingement of multiple vortex rings on a solid surface are composed of mutual interactions of vortex rings and the interactions of a vortex ring with a wall. The behavior of two coaxial vortex rings with the same sense of rotation has been extensively studied [4–6]. Under inviscid conditions, a leapfrogging behavior is predicted due to the mutual interactions of the velocity fields of the two rings [4]. However, for viscous flows, the behavior depends on the Reynolds number, the initial separation, and the core thickness of the rings [5,6]. Low Reynolds numbers and small initial separation between the rings cause the rings to coalesce without leapfrogging. At higher Reynolds numbers and higher initial separation, a finite number of leap-frogging cycles are observed before core distortion and viscous dissipation causes the rings to merge into a single ring. The effect of these parameters has been studied in literature [6]. The interaction of a vortex ring with a solid wall can be understood by separating the inviscid and viscous interactions. The inviscid interaction of a vortex ring can be modeled using the image-plane technique [7] (i.e., two vortex rings of opposite circulation approaching each other along a common axis). The mutual interaction of the velocity fields causes the rings to expand, and consequently the rate of approach decreases. Thus, a vortex ring asymptotically approaches an inviscid wall while expanding outward. In presence of viscosity, along with the inviscid effects, the velocity field of the vortex induces a boundary-layer vorticity with an opposite sense of circulation. As the ring approaches the wall, the surface vorticity layer intensifies and eventually ejects a secondary vortex ring. Depending on the Reyn-olds number, the ejection of a tertiary ring is also possible. The induced velocity fields of the secondary and tertiary rings affect the trajectory of the primary ring near the wall. The secondary and tertiary rings roll up around the primary ring and may eventually coalesce. Several experimental and computational investigations focusing on the normal impingement of a vortex ring on a solid wall have reported these flow physics [7–12].

In the present study, the incompressible Navier–Stokes equations [13] are solved numerically to simulate vortex-dominated flows.

*Graduate Research Assistant, Applied Mathematics & Statistics, and Scientific Computation; ghosh@umd.edu. Student Member AIAA.

†Associate Professor, Department of Aerospace Engineering; baeder@umd.edu. Associate Fellow AIAA.

These equations have been formulated in various forms [13,14], which include the primitive variable formulation, the pressure-Poisson formulation, the vorticity transport formulation, and the vorticity–stream-function formulation. These formulations are mathematically equivalent if physically relevant initial and boundary conditions satisfying mass continuity are specified. The primitive variable formulation has been adopted for its relative simplicity in the current work. It provides a straightforward representation of the Navier–Stokes equations, and the implementation of boundary conditions on primitive variables is relatively intuitive.

The numerical methods for the primitive variable formulation can be classified into three broad categories. One of them is the family of schemes with implicit pressure correction [15], and these have been applied to steady or quasi-steady problems where time accuracy is not required. Another family of numerical methods is the artificial compressibility methods [16,17], which cast the governing equations in a form similar to that of the compressible Navier–Stokes equations by introducing an artificial density variable. Although this allows the application of numerical schemes developed for the compressible flow equations to the incompressible ones, it introduces an arbitrary parameter. Satisfaction of mass continuity renders the system of equations stiff for unsteady problems. The projection schemes or the fractional-step schemes [18–20] have been reported to be the best suited for time-accurate computations of unsteady flows. These methods are based on the splitting of a vector field into its solenoidal and nonsolenoidal components. A predicted velocity field is computed based on the convective and diffusive terms, and a pressure-based correction is used to enforce the divergence-free condition of mass conservation. In the present study, the fractional-step method is used because the algorithm is primarily intended for simulation of unsteady flows.

Although the incompressible Navier–Stokes equations do not admit discontinuous solutions, steep gradients may develop in flows with strong shear layers and concentrated vortices. In the low-Reynolds-number regime, central differencing of spatial derivatives is sufficient to give satisfactory results [20] because the viscosity present in the system dampens the oscillatory behavior of central schemes. At higher Reynolds numbers, upwinding is required to prevent spurious oscillations. A primitive variable algorithm based on an upwind flux reconstruction and weighted essentially nonoscillatory (WENO) interpolation has been presented [21]. It uses a nonconservative form of the convective term and discretizes it in an upwind fashion. In the present study, a Cartesian staggered-grid solver is developed based on the fractional-step algorithm. A high-order spatial reconstruction is used for convective fluxes with WENO limiting while the viscous terms are treated with second-order central differences. An upwinding procedure for the conservative flux formulation is proposed for a staggered mesh where the velocity components are stored at different points. The two formulations for the convective flux are mathematically identical under the condition that the incompressible continuity equation is exactly satisfied. However, in numerical solutions, there is a finite nonzero divergence present in the computed solution, and thus differences are expected between solutions resulting from using the conservative and nonconservative formulations. An effort is made to study and document these differences.

The numerical algorithm is verified for benchmark incompressible flow problems as well as vortex-dominated flows for which results are available in literature. The lid-driven square cavity [22] and the double shear layer test [23] are benchmark cases for viscous and inviscid incompressible flows, respectively. The performance of the algorithm is studied by solving the convection of an isolated vortex for which the exact solution is available. For this problem, solutions obtained using the conservative flux formulation in the present algorithm are compared against those obtained using the non-conservative flux formulation. The mutual interactions of coplanar [24] and coaxial vortex rings [4] are studied, and the results are verified. The algorithm is used to simulate viscous interactions of vortical structures with a solid wall. A two-dimensional interaction of a vortex dipole with a wall [25,26] is studied because it encapsulates many of the flow features of a vortex ring interacting

with a wall (except the ring expansion and consequent core shrinking). The interaction of a vortex ring with a solid wall is studied at two different Reynolds numbers, and the results are compared with those in literature [11]. Based on these results, an attempt is made to study the interactions of two and multiple rings with a solid wall, which are believed to be a combination of the aforementioned behaviors. Results are shown for different Reynolds numbers and initial separations, and an attempt is made to understand the effect of these parameters on the flow.

II. Methodology

A. Governing Equations

The incompressible Navier–Stokes equations are obtained by assuming density to be constant in the generalized Navier–Stokes equations for compressible flow. The conservation of mass results in a divergence-free condition for the velocity field, expressed as

$$\frac{\partial u_i}{\partial x_i} = 0 \tag{1}$$

The momentum equations are expressed as

$$\frac{\partial u_i}{\partial t} + \frac{\partial (u_i u_j)}{\partial x_j} = -\frac{\partial p}{\partial x_i} + \nu \frac{\partial^2 u_i}{\partial x_j \partial x_j} \tag{2}$$

The incompressibility condition causes the energy equation to be decoupled from the system and is not solved as a part of the main solution algorithm in the present study. The divergence-free condition for the velocity can be used to express the momentum equations as

$$\frac{\partial u_i}{\partial t} + u_j \frac{\partial u_i}{\partial x_j} = -\frac{\partial p}{\partial x_i} + \nu \frac{\partial^2 u_i}{\partial x_j \partial x_j} \tag{3}$$

Equation (2) uses a conservative form of the convective terms, whereas Eq. (3) uses a nonconservative form. They are identical if Eq. (1) is exactly satisfied.

B. Numerical Method

The fractional-step algorithm [20] is used to integrate the governing equations in time. The predictor step involves the calculation of a velocity field $\mathbf{u}^*$ based on the convective and diffusive terms in Eqs. (2) and (3). The corrector step is then used to compute a pressure field consistent with the continuity equation given by Eq. (1). The predicted velocity $\mathbf{u}^*$ is then corrected to ensure that the solution at the next time step is divergence-free.

To prevent the pressure–velocity decoupling seen in collocated variable algorithms, the equations are discretized and solved on a staggered mesh. If (i, j, k) are the mesh indices corresponding to (x, y, z) axes, respectively, then u (x velocity) is stored at $(i + 1/2, j, k)$; v (y velocity) is stored at $(i, j + 1/2, k)$; and w (z velocity) is stored at $(i, j, k + 1/2)$.

The momentum equations excluding the pressure terms are solved in the predictor step. For the conservative form given by Eq. (2), the predictor step computes the solution of the following system of equations:

$$\begin{bmatrix} u \\ v \\ w \end{bmatrix}_t + \begin{bmatrix} u^2 \\ uv \\ uw \end{bmatrix}_x + \begin{bmatrix} uv \\ v^2 \\ vw \end{bmatrix}_y + \begin{bmatrix} uw \\ vw \\ w^2 \end{bmatrix}_z$$

$$= \nu \begin{bmatrix} u_{xx} + u_{yy} + u_{zz} \\ u_{xx} + u_{yy} + u_{zz} \\ w_{xx} + w_{yy} + w_{zz} \end{bmatrix} \tag{4}$$

where the subscripts denote partial derivatives. The corresponding system for the nonconservative form given by Eq. (3) can be written as

$$
\begin{bmatrix} u \\ v \\ w \end{bmatrix}_t + u \begin{bmatrix} u \\ v \\ w \end{bmatrix}_x + v \begin{bmatrix} u \\ v \\ w \end{bmatrix}_y + w \begin{bmatrix} u \\ v \\ w \end{bmatrix}_z
$$
$$
= v \begin{bmatrix} u_{xx} + u_{yy} + u_{zz} \\ u_{xx} + u_{yy} + u_{zz} \\ w_{xx} + w_{yy} + w_{zz} \end{bmatrix} \tag{5}
$$

Time integration of the convective terms is carried out using either the second-order Adams–Bashforth (AB2) scheme or the low-storage third-order Runge–Kutta (RK3) scheme. The viscous terms are treated using the trapezoidal scheme to remove the restrictive time-step size limit. It should be noted that, for higher-Reynolds-number flows, explicit treatment of the viscous terms suffices.

The convective terms in the conservative flux formulation have the general form given by the second term on the left-hand side of Eq. (2), which are discretized using a conservative discretization. As an example, the discretization of the y component of the flux in the x momentum equation is

$$
\frac{\partial(uv)}{\partial y} \approx \frac{(uv)_{i+1/2,j+1/2,k} - (uv)_{i+1/2,j-1/2,k}}{y_{j+1/2} - y_{j-1/2}} \tag{6}
$$

Note that, in the staggered arrangement, the control volume of the discretized x momentum equation is centered at $(i + 1/2, j, k)$. The previous expression requires the interpolated values of u and v at $(i + 1/2, j + 1/2, k)$ and $(i + 1/2, j - 1/2, k)$. Using second-order central differences, these values can be obtained by averaging the two neighboring values:

$$
u_{i+1/2,j+1/2,k} = \frac{1}{2}(u_{i+1/2,j,k} + u_{i+1/2,j+1,k})
$$

$$
v_{i+1/2,j+1/2,k} = \frac{1}{2}(v_{i,j+1/2,k} + v_{i+1,j+1/2,k})
$$

In an upwind reconstruction for a given face, only the tangential velocity component is evaluated using a biased interpolation based on the sign of the normal velocity component. The velocity component normal to the face is computed using a centered stencil because upwinding it based on the sign of the tangential component would be nonphysical. Thus, for the previous example, u is computed at the face using a stencil centered around $u_{i+1/2,j,k}$ or $u_{i+1/2,j+1,k}$ aligned along the j index, depending on the signs of $v_{i,j+1/2,k}$ and $v_{i+1,j+1/2,k}$, i.e.,

$$
S(u_{i+1/2,j-n,k}, \ldots, u_{i+1/2,j,k}, u_{i+1/2,j+1,k}, \ldots, u_{i+1/2,j+n,k})
$$

if $v_{i,j+1/2,k}, v_{i,j+1/2,k} > 0$

$$
S(u_{i+1/2,j-n+1,k}, \ldots, u_{i+1/2,j,k}, u_{i+1/2,j+1,k}, \ldots, u_{i+1/2,j+n+1,k})
$$

if $v_{i,j+1/2,k}, v_{i,j+1/2,k} < 0$

$$
S(u_{i+1/2,j-n+1,k}, \ldots, u_{i+1/2,j,k}, u_{i+1/2,j+1,k}, \ldots, u_{i+1/2,j+n,k})
$$

otherwise

This results in a $(2n + 1)$th-order upwind interpolation or a $(2n)$th-order central interpolation if the face normal velocity component changes sign. The interpolated value of v at the face, $v_{i+1/2,j+1/2,k}$, is computed using a centered stencil aligned along the i index, i.e., $S(v_{i-n+1,j+1/2,k}, \ldots, v_{i,j+1/2,k}, v_{i+1,j+1/2,k}, \ldots, v_{i+n,j+1/2,k})$ for a $(2n)$th-order interpolation. If an rth-order biased stencil is used to compute the upwinded velocity component, an $(r - 1)$th-order centered interpolation is used to compute the other component.

The general form of the convective flux terms in the non-conservative formulation is given by the second term on the left-hand side of Eq. (3). The second-order central scheme is equivalent to simple averaging. For an upwind scheme, the velocity component inside the derivative is upwinded based on the sign of the velocity component outside the derivative [21]. The discretization of the y component of the flux in the x momentum equation is considered. The discretized form of this term is

$$
v \frac{\partial u}{\partial y} \approx v_{i+1/2,j,k} \frac{u_{i+1/2,j+1/2,k} - u_{i+1/2,j-1/2,k}}{y_{j+1/2} - y_{j-1/2}} \tag{7}
$$

Thus, u is interpolated at $(i + 1/2, j + 1/2, k)$ using a stencil centered at $(i + 1/2, j, k)$ or $(i + 1/2, j + 1, k)$ based of the signs of $v_{i,j+1/2,k}$ and $v_{i+1,j+1/2,k}$. It should be noted that the value of v is required at $(i + 1/2, j, k)$ and is computed using a centered two-dimensional stencil of the appropriate order. An $(r - 1)$th-order centered interpolation is used for the nonupwind component if an rth-order interpolation is used for the upwind component.

The aforementioned velocity components are evaluated using high-order interpolations. In the present study, fifth-order interpolation is used, with and without WENO limiting [27], for the upwind velocity components. A fourth-order central interpolation is used for normal velocity components at each interface. The spatial derivatives in the viscous terms are approximated using second-order central differencing. Along with the trapezoidal scheme in time, they form a system of equations that is solved using the strongly implicit procedure (SIP) [28]. The system is diagonally dominant and converges (residual drop to machine zero) within a few subiterations. Thus, implicit treatment of the viscous terms does not substantially increase the time of computation and is retained even for higher-Reynolds-number cases.

The predicted velocity field $\mathbf{u}^*$ may have a nonzero divergence, which needs to be corrected to satisfy mass conservation. Considering the pressure gradient terms that were omitted from Eqs. (4) and (5) and discretizing in time, the corrector step is expressed as

$$
\frac{\mathbf{u}^{n+1} - \mathbf{u}^*}{dt} = -\nabla \phi \tag{8}
$$

where ϕ is the solution of the Poisson equation given by

$$
\nabla^2 \phi = \frac{1}{dt} \nabla . \mathbf{u}^* \tag{9}
$$

It should be noted that ϕ is a mathematical variable used to enforce mass continuity and is not the physical pressure [14,20]. In the staggered-mesh arrangement, it is stored at (i, j, k) locations. Second-order central differences are used for all derivatives in the previous two equations. This results in a system of equations that is solved iteratively using the SIP. The system is not as diagonally dominant as the one in the predictor step and thus requires a larger number of subiterations for the residual to fall few orders of magnitude. Equation (8) is used to obtain the velocity at the next time level.

III.   Algorithm Verification

The upwind, conservative flux-based algorithm described in the previous section is verified for benchmark problems in incompressible flow as well as vortex-dominated flows. The lid-driven square cavity is a test case for viscous incompressible flows and is solved at various Reynolds numbers. The results are compared with those in literature. The double shear layer problem is solved to study the performance of the algorithm at the inviscid limit, and the upwind schemes are shown to yield nonoscillatory results. The convection of an isolated vortex is simulated to analyze the performance of the various schemes because an exact solution is available in analytical form. The results from the proposed algorithm using a conservative flux formulation are compared with results obtained using a nonconservative flux formulation. A difference in the solutions is observed due to the numerical error in satisfying mass conservation.

The conservative algorithm is used to model flows involving the convection, mutual interactions, and the interactions with solid surfaces of vortical structures. The results are compared and verified with theoretical predictions and computational results in literature. Two cases involving the mutual interaction of vortex rings are studied: the viscous interaction of two coplanar vortex rings and the inviscid leapfrogging of two coaxial, corotating vortex rings. The results from the coplanar vortex ring interaction case are compared
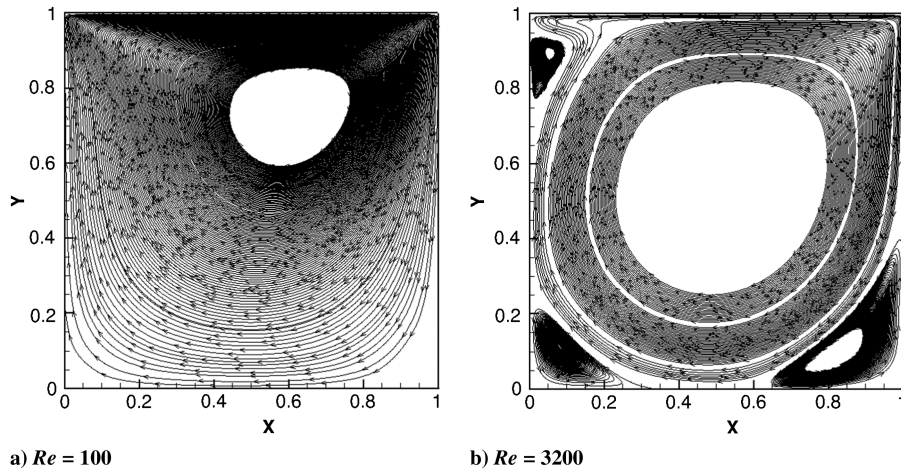
a) *Re* = 100   b) *Re* = 3200

Fig. 1 Streamlines for lid-driven square cavity.

with those in literature, while the inviscid leapfrogging case demonstrates the performance of the algorithm for flows involving concentrated vortical structures with steep gradients. Problems involving the viscous interactions of vortices with a solid surface are studied, and the results are compared with experimental/ computational results that have been previously published. The two-dimensional vortex dipole rebound from a solid wall is studied because it is a simplified representation of the three-dimensional ring impingement lacking the core straining that occurs for an expanding or contracting vortex ring. The interaction of a single vortex ring with a solid wall is studied at two different Reynolds numbers, and good agreement is observed with previous studies.

A. Lid-Driven Square Cavity

This test problem deals with the flow inside a square cavity with uniform horizontal flow or a moving lid covering the cavity. The flow is characterized by a primary vortex and up to three secondary vortices depending on the Reynolds number. Several computational solutions are available for this problem in literature, thus making this a benchmark problem. The domain is a unit square ($[0, 1] \times [0, 1]$). The initial condition consists of a clockwise rotating vortex given by

$$u = y - 0.5 \qquad v = -(x - 0.5)$$

Solid boundary conditions are imposed on the bottom, left, and right boundaries, while a unit horizontal velocity $u = 1$, $v = 0$ is imposed on the top boundary. A zero normal gradient is imposed for pressure on all boundaries. The solution is marched in time until it reaches a steady state (i.e., the separation and attachment points of the secondary vortices become fixed).

Figure 1 shows the streamlines of the flow at two different Reynolds numbers. At a Reynolds number of 100, only the primary vortex is present, whereas, at a higher Reynolds number of 3200, secondary and tertiary vortices are observed. These observations are consistent with those in literature [22]. Figure 2 shows the horizontal and vertical velocity profiles through the center of the domain for Reynolds numbers of 100 and 3200. All computations are carried out on a 130×130 grid. The results obtained using the second-order central scheme and fifth-order upwind scheme are compared with previous results [22]. AB2 time stepping is used with second-order reconstruction of the convective terms, while RK3 time stepping is used for fifth-order spatial reconstruction. Good agreement is observed between the present results and the accepted ones. It can
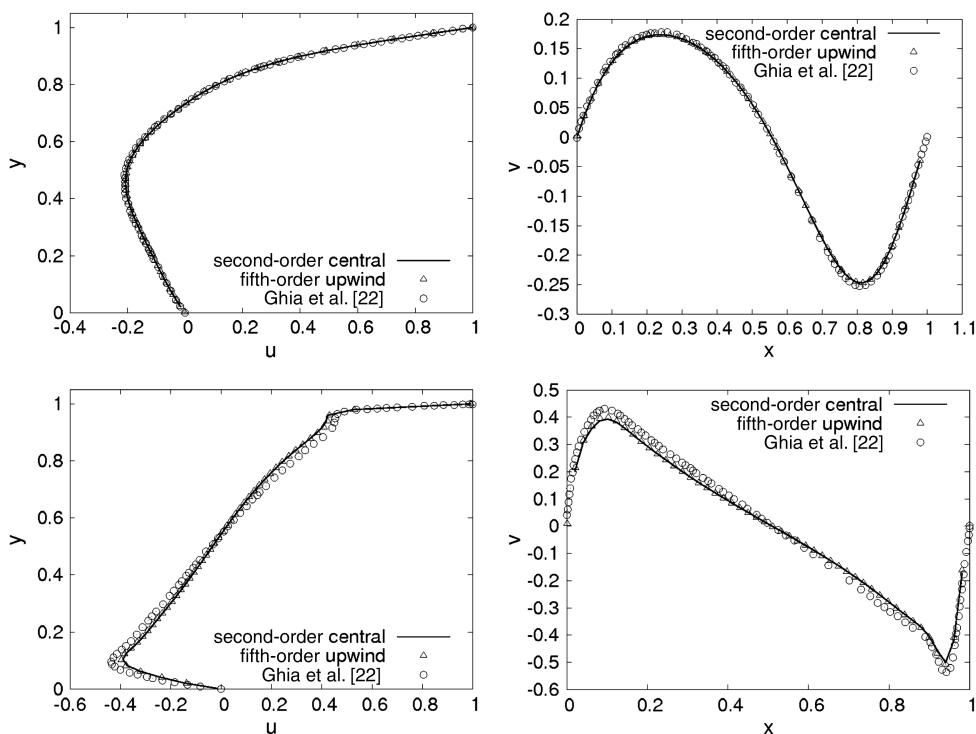

Fig. 2 Cross-sectional velocity profiles for Reynolds numbers 100 and 3200.

also be observed that, in this case, where Reynolds numbers are relatively low, the second-order central solutions and the fifth-order upwind solutions are identical.

B.   Double Shear Layer Test

The double shear layer test is a standard benchmark case for an inviscid, incompressible flow solver [21,23]. The initial flow consists of two shear layers with finite but small thickness. In the present study, the 'thick' version of the shear layer test is solved because it is more suitable for verification. The velocity field is given as [23]

$$u(x, y) = \tanh\left[\frac{1}{\rho}\left(y - \frac{\pi}{2}\right)\right], \qquad y < \pi$$
$$= \tanh\left[\frac{1}{\rho}\left(\frac{3\pi}{2} - y\right)\right], \qquad y \geq \pi$$
$$v(x, y) = \delta \sin(x)$$

In the present case, the value of the thickness parameter ρ is taken as $\pi/15$. The perturbation parameter for the v velocity component δ is taken as 0.05. The domain is the square of the length 2π and periodic

boundary conditions are applied on all boundaries. The evolution of the flowfield is studied until a final time of $t = 14$. Figure 3 shows the evolution of the flow computed on a 256×256 grid using fifth-order WENO interpolation and RK3 time stepping. The results agree well with those in literature [21,23].

Figure 4 compares the different spatial schemes for this problem on a 128×128 grid. The second-order central scheme yields extremely oscillatory results, thus reiterating that upwinding is required to obtain a nonoscillatory solution in the inviscid limit. The fifth-order schemes yielded similar results with and without WENO limiting, despite this problem having very steep gradients. However, further tests need to be carried out for more complicated problems to determine if WENO limiting is necessary or if upwinding the flux provides sufficient stability. Figure 5 shows the evolution of the kinetic energy (normalized with the initial kinetic energy) for the different schemes on a 128×128 grid. The conservative flux formulation is compared with the nonconservative flux formulation and is observed to be more dissipative. The solutions obtained with WENO limiting are slightly more dissipative than those obtained with the fifth-order schemes for both formulations. The error in the kinetic energy is 0.025–0.03 for the nonconservative formulation and 0.035–0.04 for the conservative flux formulation. These compare well with the results presented in literature [21].
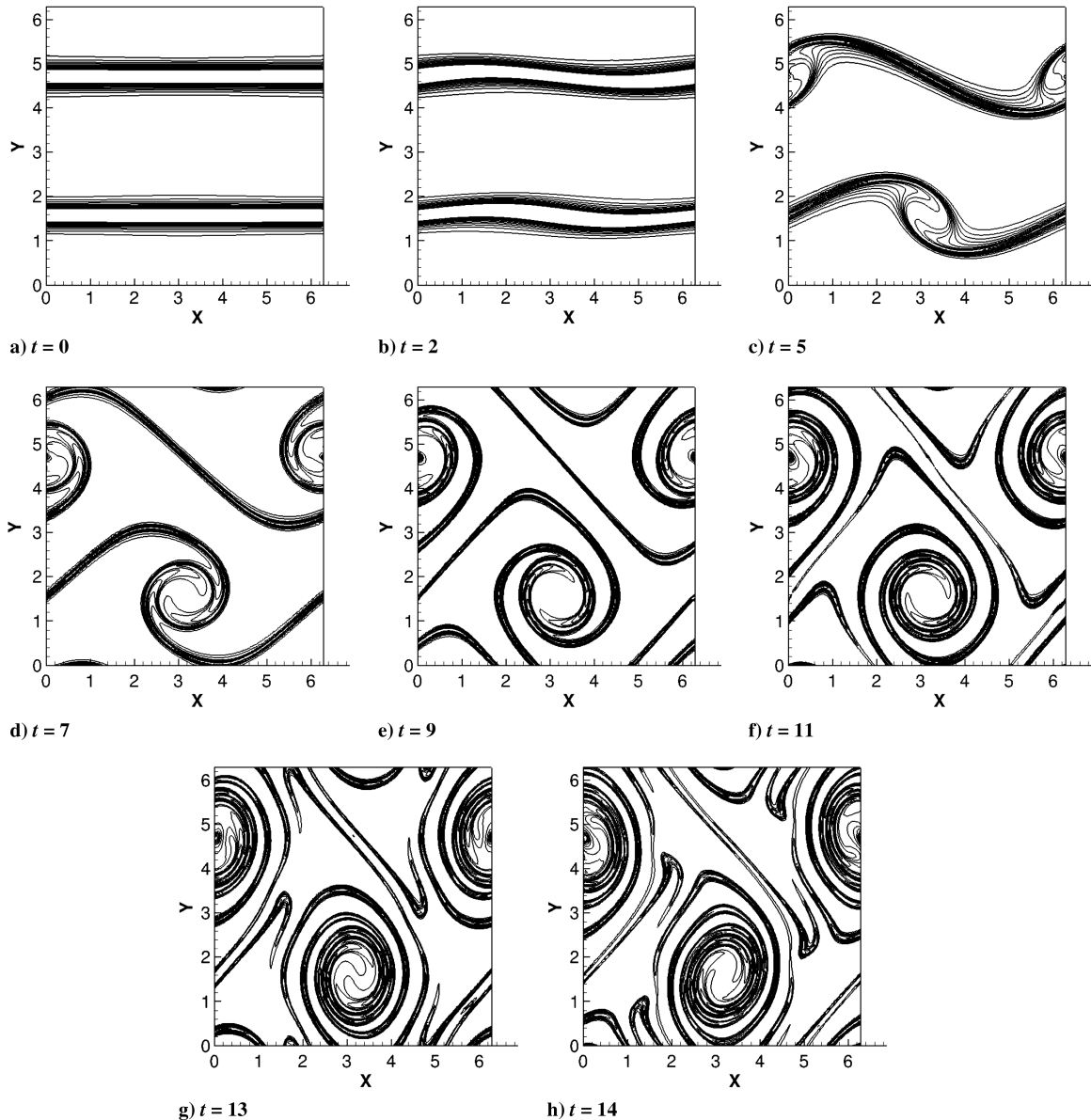

a) $t = 0$ b) $t = 2$ c) $t = 5$

d) $t = 7$ e) $t = 9$ f) $t = 11$

g) $t = 13$ h) $t = 14$

Fig. 3   Evolution of double shear layer.

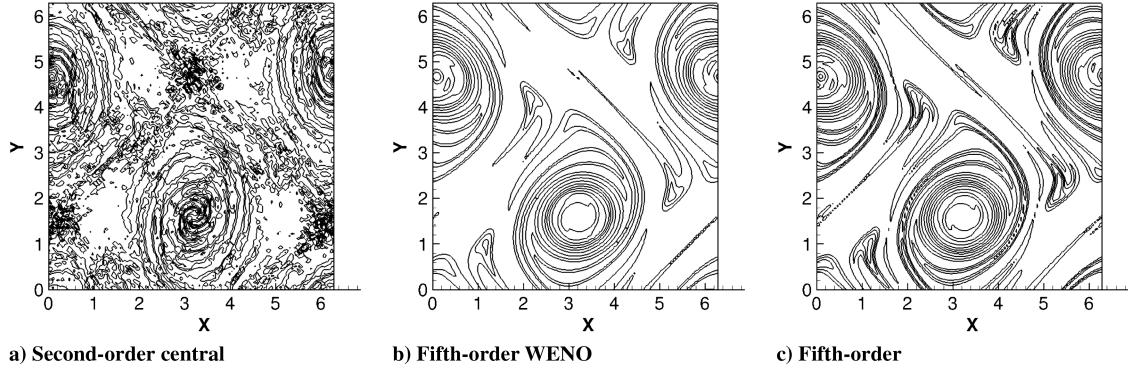a) Second-order central　　　　　　　b) Fifth-order WENO　　　　　　　c) Fifth-order
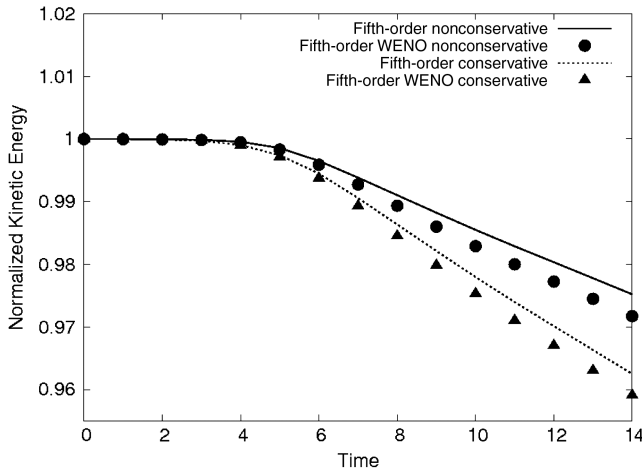
Fig. 4　Comparison of schemes; double shear layer.

Fig. 5　Evolution of normalized kinetic energy for different schemes.

C.　Taylor Vortex Convection

The convection of an isolated vortex is studied in this problem. The Taylor vortex is an exact solution of the Navier–Stokes equations, and its analytical form is given as [25]

$$u = \frac{-(y - y_c)}{1 + 2t/Re} \exp\left[\frac{1}{2}\left(1 - \frac{(x - x_c)^2 + (y - y_c)^2}{1 + 2t/Re}\right)\right] + U$$

$$v = \frac{(x - x_c)}{1 + 2t/Re} \exp\left[\frac{1}{2}\left(1 - \frac{(x - x_c)^2 + (y - y_c)^2}{1 + 2t/Re}\right)\right]$$

The Reynolds number is defined as $Re = u_{\theta 0} r_0 / \nu$ ($u_{\theta 0}$ is the maximum azimuthal velocity at time $t = 0$ and r_0 is the initial radius of the vortex). The domain is $[-8, 8] \times [-8, 8]$, and the convection

velocity is $U = 8$. Thus, with periodic boundary conditions, the time period is 2. The vortex is initially located at the center of the domain ($x_c = y_c = 0$ at $t = 0$).

The inviscid and viscous convection of the vortex is studied. Solutions obtained from the present solver using a conservative flux formulation are compared with those obtained using a nonconservative flux formulation for second-order central, fifth-order upwind, and fifth-order upwind WENO interpolations. Time integration for the convective terms is carried out using the RK3 scheme. Viscous convection of the vortex is studied at a Reynolds number of 100. Figure 6a shows the v velocity profile through the vortex core after one pass over the periodic domain on a 128×128 grid. The solutions for each pass are obtained at integer multiples of the time period. It is observed that, for all orders, the nonconservative flux formulation is significantly less dissipative. There is an underprediction of the convection speed. At a relatively low Reynolds number, the second-order central and fifth-order upwind solutions are identical.

Figure 6b shows the v velocity profile of the convecting vortex for the inviscid case after three passes over the domain. Results are not shown for second-order central interpolation because they are too oscillatory to yield a meaningful solution. The fifth-order upwind schemes, with and without WENO limiting, are compared for both the conservative and nonconservative flux formulations. The schemes using the nonconservative flux formulation are observed to be less dissipative than the conservative ones. However, they contain a larger error in the convection speed of the vortex. The solution for this problem is smooth, and there is only slight difference between fifth-order upwind schemes with and without WENO limiting.

Successive grid refinement is used to assess the order of convergence for the various schemes. Errors are shown for third- and fifth-order WENO schemes with conservative flux formulation (WENO3 conservative and WENO5 conservative) and with nonconservative flux formulation (WENO3 nonconservative and
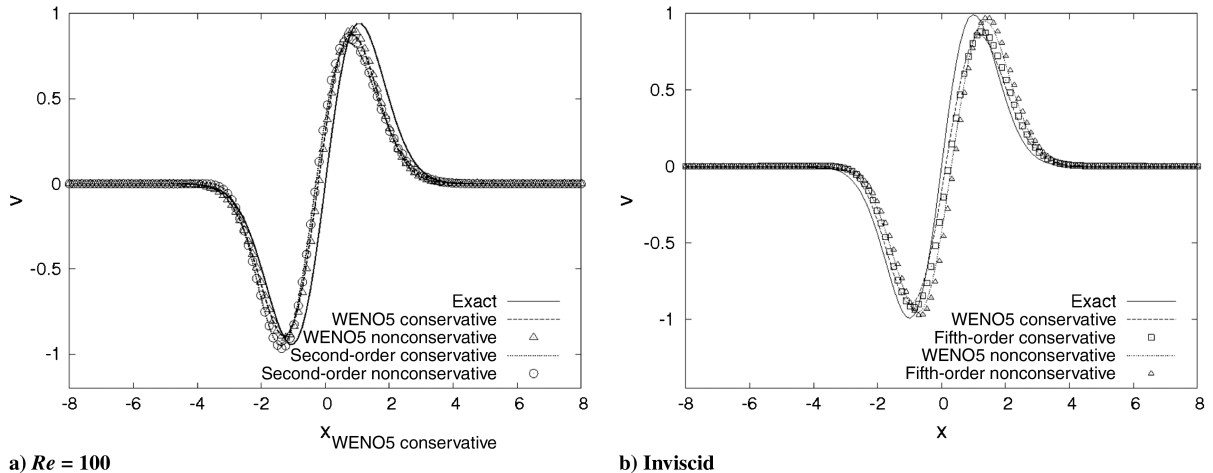

a) Re = 100　　　　　　　　　　　　　　　b) Inviscid

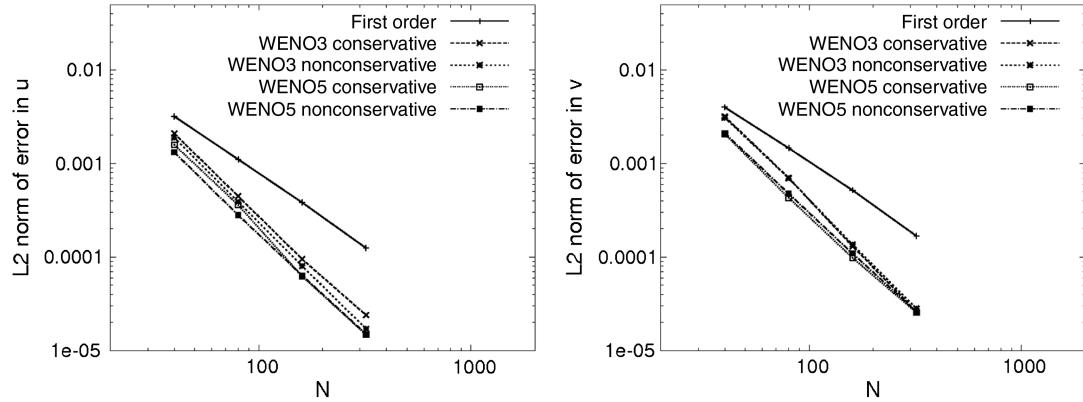Fig. 6　Taylor vortex convection over a periodic domain.

Fig. 7   Convergence of various schemes for vortex convection problem.

WENO5 nonconservative). The inviscid convection of the vortex is considered. Figure 7a shows the L_2 norm of the error in the u velocity after one pass over the domain. The grid is refined from 40×40 to 320×320. Figure 7b shows the same for the v velocities. The higher-order schemes achieve a convergence rate of around $\mathcal{O}(N^2)$, which is less than the formal order of accuracy of the interpolations used in flux reconstruction. Although the third- and fifth-order WENO schemes show similar orders of convergence, the absolute errors are less for higher-order interpolation. The Poisson solution in the corrector step is solved using second-order spatial differencing, and this could be the limiting factor. The conservative and non-conservative schemes have similar orders of convergence, though the nonconservative flux formulation results in lower absolute errors for this problem. This would indicate that the accuracy of the Poisson solver in the corrector step is decisive to the overall algorithm because the difference between the two flux formulations is the numerical error in satisfying mass conservation.

D.   Coplanar Vortex-Ring Interaction

A three-dimensional problem involving the collision of two vortex rings in space is used to verify the algorithm for viscous vortex interactions. Vortex interactions of this nature have been extensively studied [24] and can thus be used as a benchmark case. The initial flow consists of two vortex rings, each with a Gaussian azimuthal vorticity distribution given by [25]

$$\omega(x, y, z) = \omega_0 \exp\left[-\left(\frac{r}{a}\right)^2\right] \qquad (10)$$

where $r = [(x - x_c)^2 + (y - y_c)^2 + z^2]^{\frac{1}{2}}$ is the radial distance from the center of the cross section. The domain is a cube of length 2π. The cross section of each ring is centered at $x_c = X_c + R\cos\theta$,

$y_c = Y_c + R\sin\theta$, where X_c, Y_c are the coordinates of the center of the vortex ring lying in the $z = 0$ plane; R is the radius of the vortex ring; θ is the azimuthal angle in the x–y plane; and a is the thickness of the ring. The rings are centered at $(\pm\frac{1}{2}D\cos(\pi/4)$, $\pm\frac{1}{2}D\sin(\pi/4))$, resulting in a separation distance of D between their centers. In the present study, the values for these parameters are $D = 1.83$, $R = 0.491$, $a = 0.196$, and $\omega_0 = 23.8$ [25]. Figure 8 shows the time evolution of the vortex rings interaction for a circulation based Reynolds number of 577 ($Re = \pi\omega_0 a^2/\nu$); the normalized vorticity magnitude isosurfaces are plotted. The domain is discretized by a $128 \times 128 \times 128$ grid. The results shown are obtained using fifth-order upwind scheme and RK3 time stepping. Similar results are obtained using second-order central scheme with AB2 time stepping. These are in good agreement with those in literature [24,25].

E.   Leapfrogging Motion of Corotating Vortex Rings

In this problem, the inviscid interaction between two coaxial vortex rings with the same sense of circulation is studied. A leapfrogging motion of two rings around each other is predicted for large, thin rings in the inviscid limit [4]. The trailing ring contracts and slips through the leading ring. This motion repeats indefinitely for inviscid flows. In the presence of viscosity, the strength of the vortex rings gradually decrease, and they eventually coalesce to form a single ring due to the mutual interactions. The ratio of the core radius to the ring diameter, initial separation, and the Reynolds number determine the number of leapfrogging cycles before the rings coalesce into a single ring [5]. Thicker rings tend to coalesce sooner, whereas large, thin rings leapfrog around each other for longer times.

In the present case, the initial flow consists of two identical rings, each with a Gaussian azimuthal vorticity distribution along the core cross section given by
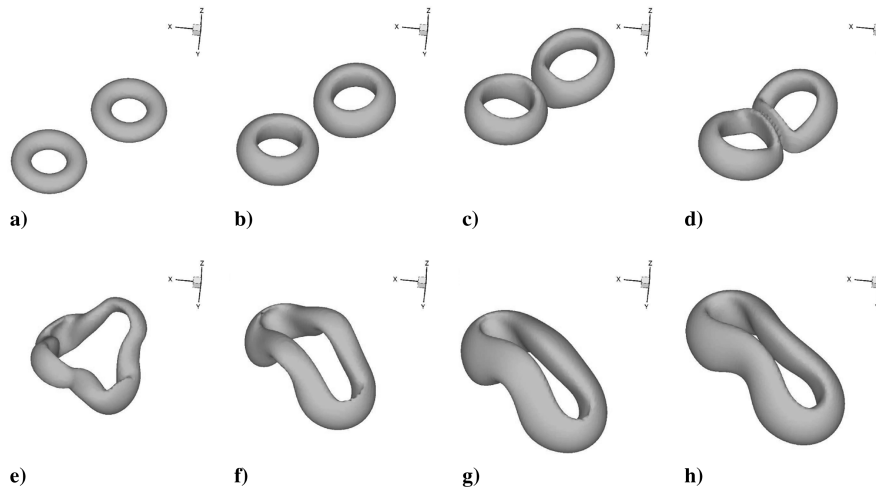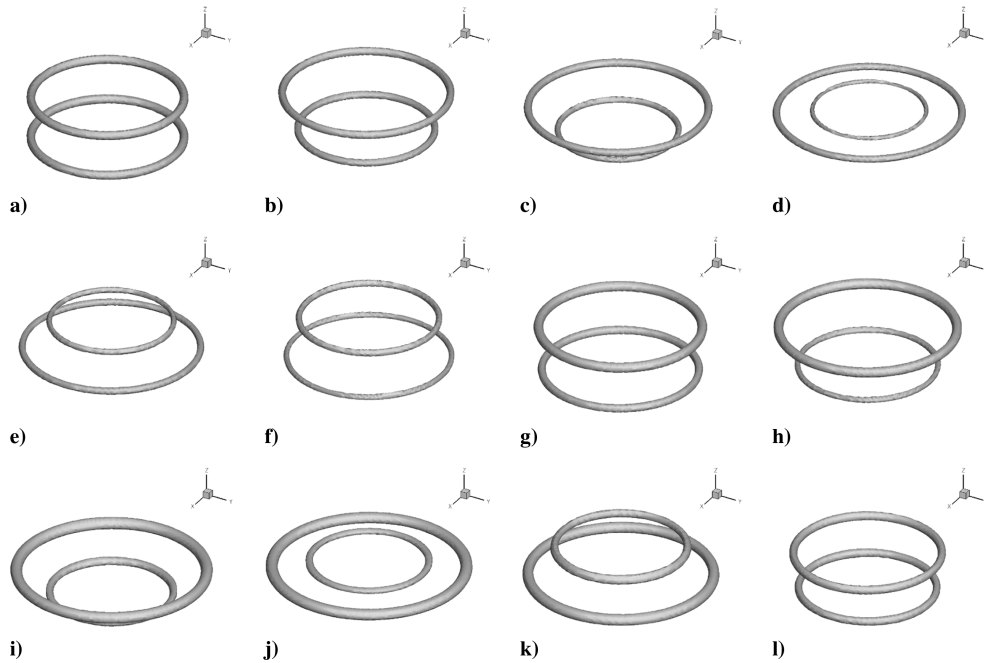

Fig. 8   Interaction of coplanar vortex rings.

Fig. 9   Leapfrogging of coaxial vortex rings.

$$\omega(x, y, z) = \frac{1}{\pi a^2} \exp\left[-\left(\frac{r}{a}\right)^2\right] \qquad (11)$$

where ω is the vorticity magnitude along the normal to the cross section, r is the distance from the center of the core, and a is the core radius. A ring thickness a/R of 0.05 is used. A cubic domain of side $5R$ is chosen with periodic boundary conditions on all boundaries, and the initial separation between the rings is taken as $0.6R$. A $144 \times 144 \times 144$ grid is used to discretize the domain, and results are obtained using the fifth-order WENO scheme and RK3 time stepping. Figure 9 shows the leapfrogging behavior for one complete cycle. The isosurfaces of the vorticity magnitude are plotted, and the

ring structure is preserved without significant dissipation. The algorithm is seen to accurately capture the leapfrogging behavior, and its performance for flows with concentrated vorticity is demonstrated.

F.   Vortex Dipole Rebound from Solid Wall

The interaction of a vortex dipole with a wall [26] illustrates many of the mechanisms seen in the interaction of a vortex ring with a wall. As the vortex dipole approaches the solid surface, it induces a surface vorticity of the opposite sign in the boundary layer. The problem is characterized by the ejection of secondary and tertiary vortices,
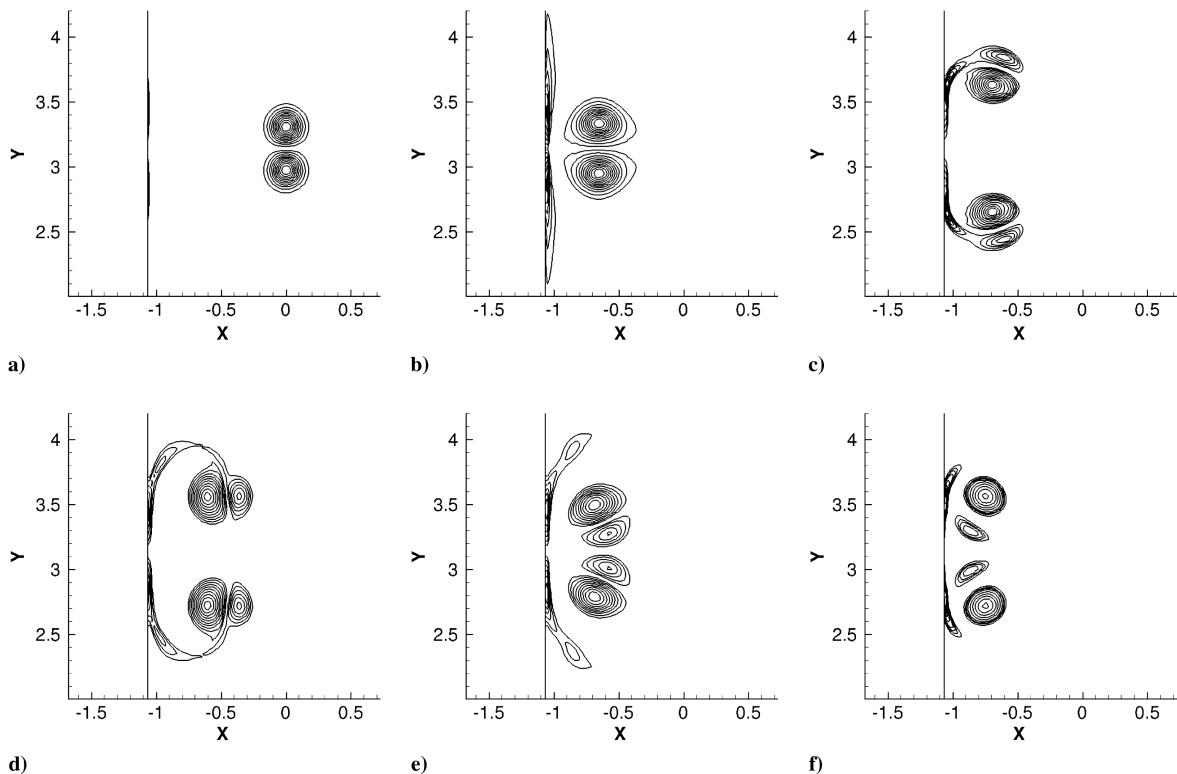

Fig. 10   Rebound of vortex dipole from wall at Reynolds number of 1800.

which then interact with the primary vortices. In the present study, the flow is initialized as a vortex dipole in stagnant flow with a Gaussian vorticity distribution given as

$$\omega(x, y) = \pm \frac{1}{\pi a^2} \exp\left[-\frac{(x - x_c)^2 + (y \pm y_c)^2}{a^2} \right] \qquad (12)$$

where the x axis is along the normal to the wall. The vortices are centered at $(x_c, \pm y_c)$ with a core radius of a. The problem is solved at a circulation based Reynolds number ($Re = 1/\nu$) of 1800. The domain is specified as $-D \leq x \leq D$ and $0 \leq y \leq 2\pi D$, and the initial separation of the vortices is $D/3$ [25]. The core radius of the vortices is $a = D/9$. The problem is solved on a 128×256 mesh. Periodic boundary conditions are applied at $y = 0, 2\pi D$; solid wall boundary conditions are applied at $x = -D$; and extrapolation is used at $x = D$.

Figure 10 shows the evolution of the problem using second-order central spatial discretization and AB2 time stepping. The out-of-plane vorticity contours are plotted. It can be seen that the primary vortices induce a boundary-layer vorticity region as they approach the wall. The boundary-layer vorticity, having an opposite sense of circulation, causes the primary vortices to move apart. They are ejected from the boundary layer as secondary vortices and interact with the primary vortices. At a later stage, tertiary vortices are also

seen to be ejected. However, the vortices diffuse with time due to the viscosity in the flow. The results agree with those in literature [25,26].

G.   Single-Vortex Ring–Wall Interaction

The impingement of a single vortex ring on solid wall is studied in this case. As the ring approaches the wall, it expands in size and induces a boundary layer at the wall. Depending on the Reynolds number, the vorticity in the boundary layer can grow until it gets ejected in the form of a secondary ring, which rolls around the primary ring. A tertiary ring ejection may also be observed for higher-Reynolds-number flows. In the present study, this interaction of the ring with a solid wall is studied at two different Reynolds numbers. The initial conditions consist of an isolated vortex ring with a cross-sectional vorticity distribution given by Eq. (11). The core radius is taken to yield a maximum vorticity magnitude of 35 for unit circulation [11]. The ring radius R is taken as $a/0.413$, and the initial height of the ring above the ground is taken as $2.4R$. The problem is simulated on a clustered mesh of dimensions $144 \times 144 \times 200$. Solid wall-boundary conditions are imposed on the bottom ($z = 0$) boundary, and extrapolation is used at all other boundaries.

The problem is simulated for two different circulation-based Reynolds numbers. Figure 11 shows the evolution of the problem at a Reynolds number of 564. The results are computed using second-order central spatial differencing and AB2 time stepping. At this low
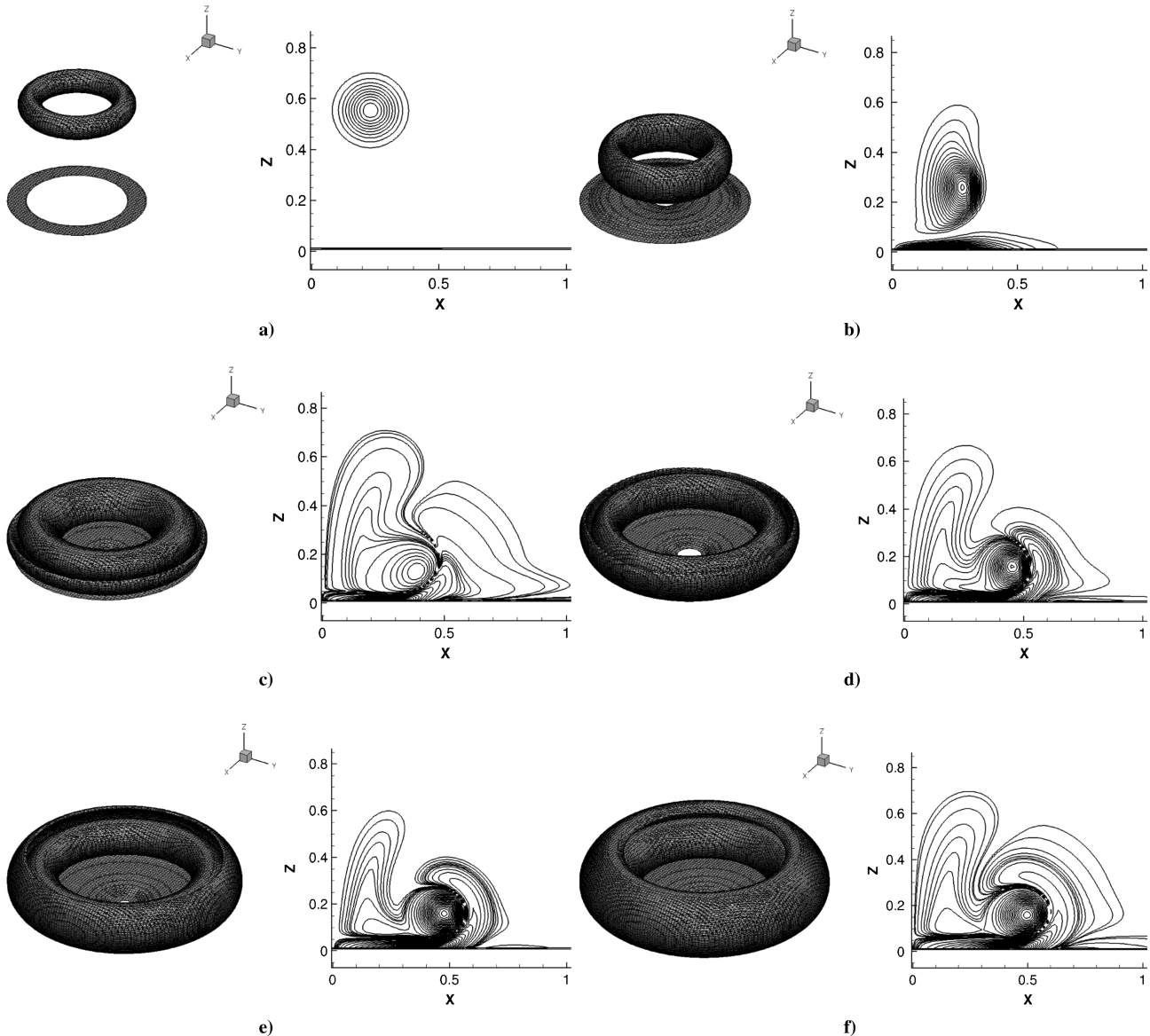

Fig. 11   Vortex ring impingement on wall at Reynolds number of 564.

Reynolds number, the ring induces a boundary-layer vorticity, which wraps around the primary ring. The left-hand side of each image shows the vorticity magnitude isosurfaces, and the right-hand side shows a contour plot of the vorticity magnitude on an azimuthal slice. The induced vorticity in the boundary layer is not strong enough to get ejected and form a separate secondary ring.

Figure 12 shows the evolution for a higher Reynolds number of 1250. The results are obtained using the fifth-order upwind WENO scheme with RK3 time stepping. At a higher Reynolds number, the induced vorticity in the boundary layer is much stronger, and the ejection and formation of a secondary ring can be clearly seen. The secondary ring circles around the primary one while a tertiary ring can be seen to be forming.

The results obtained are compared with those in literature [11], and good agreement is seen. The characteristic features of the ring-wall interactions are seen to be accurately captured.

IV. Results

The algorithm is verified on benchmark incompressible flow problems in the previous section, with particular focus on flows dominated by vortical structures. The performance of the algorithm is demonstrated for viscous as well as inviscid cases involving the mutual interaction of vortices and the interaction of a vortex ring with a solid wall. Based on these results, the simulation of multiple rings interacting with a solid wall is attempted. Initially, the interaction of two corotating, coaxial rings with a solid wall is studied. The problem is simulated at two different Reynolds numbers and initial

separations. These parameters affect the mutual interaction of the two rings in terms of leapfrogging or coalescing and thus affect the interactions with the wall. Subsequently, the simulation of multiple vortex rings interacting with a solid wall is attempted. The simulation is carried out for two different initial separations and representative results are shown.

A. Interactions of Two Rings with a Wall

The impingement of a pair of corotating vortex rings on a solid wall is studied. The approach of an isolated vortex ring toward a solid wall is characterized by the formation of a ground boundary layer and a creation of surface vorticity with an opposite sense of circulation. In the present case of two vortex rings, the initial separation and the Reynolds number affect the mutual interaction of the two rings and consequently their impingement on the wall. It is expected that, for small initial separations and at low Reynolds numbers, the two rings will coalesce to form a single ring before their impingement on the wall, and thus the flow will be similar to a single vortex-ring impingement. However, at higher Reynolds number and/or for higher initial separation, the rings will leapfrog as they impinge on the wall. The velocity field of one of the rings is expected to push the other ring toward the boundary layer, causing a stronger interaction, while the velocity field of the latter will push the former away from the wall. In the present study, the problem is studied at two different Reynolds numbers and two initial separations.

The flow is initialized for all cases as two rings, each with a cross-sectional vorticity distribution given by Eq. (11). The ring thickness a/R is 0.1, and the initial mean height is $2R$. Figure 13 shows the
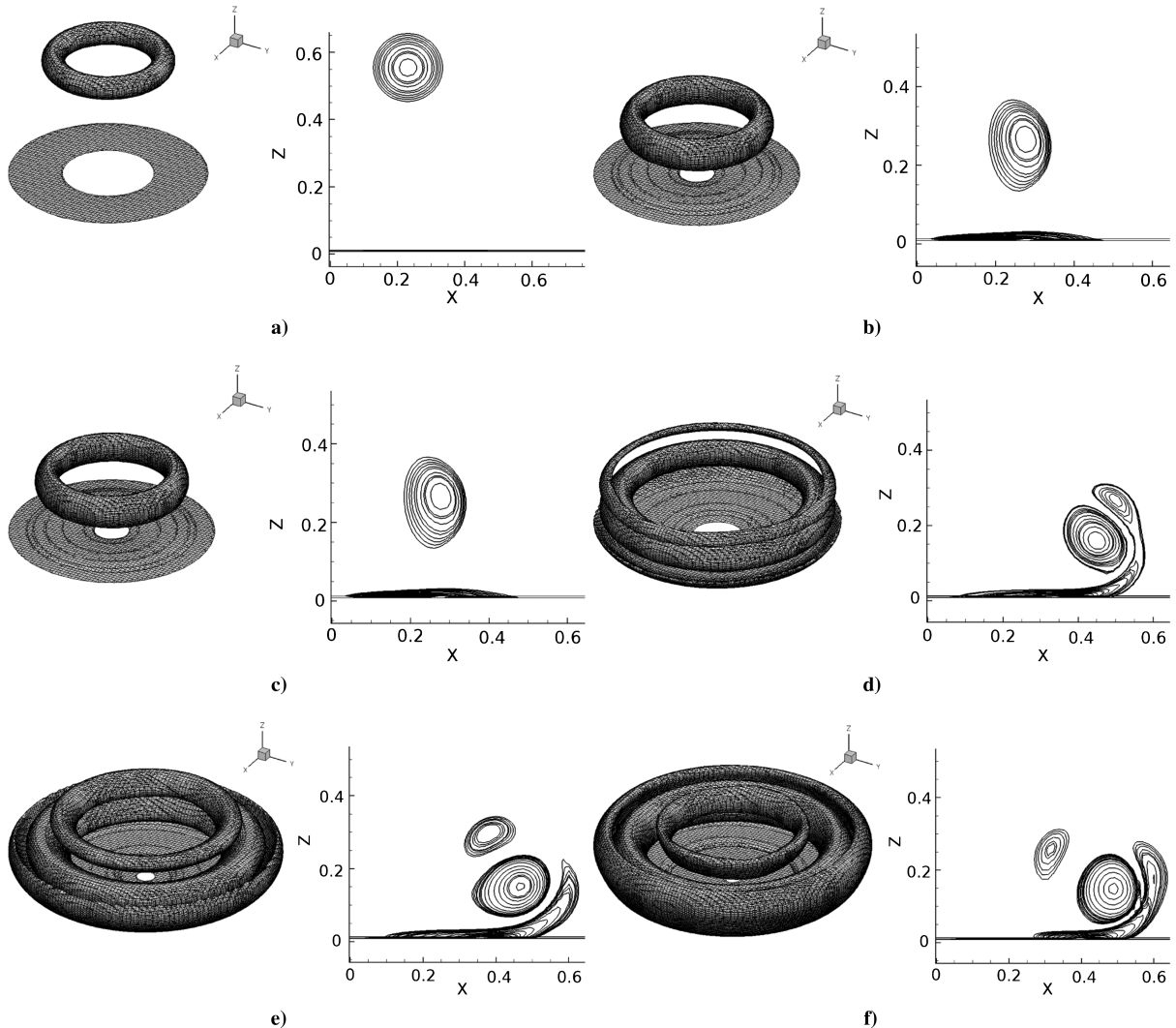

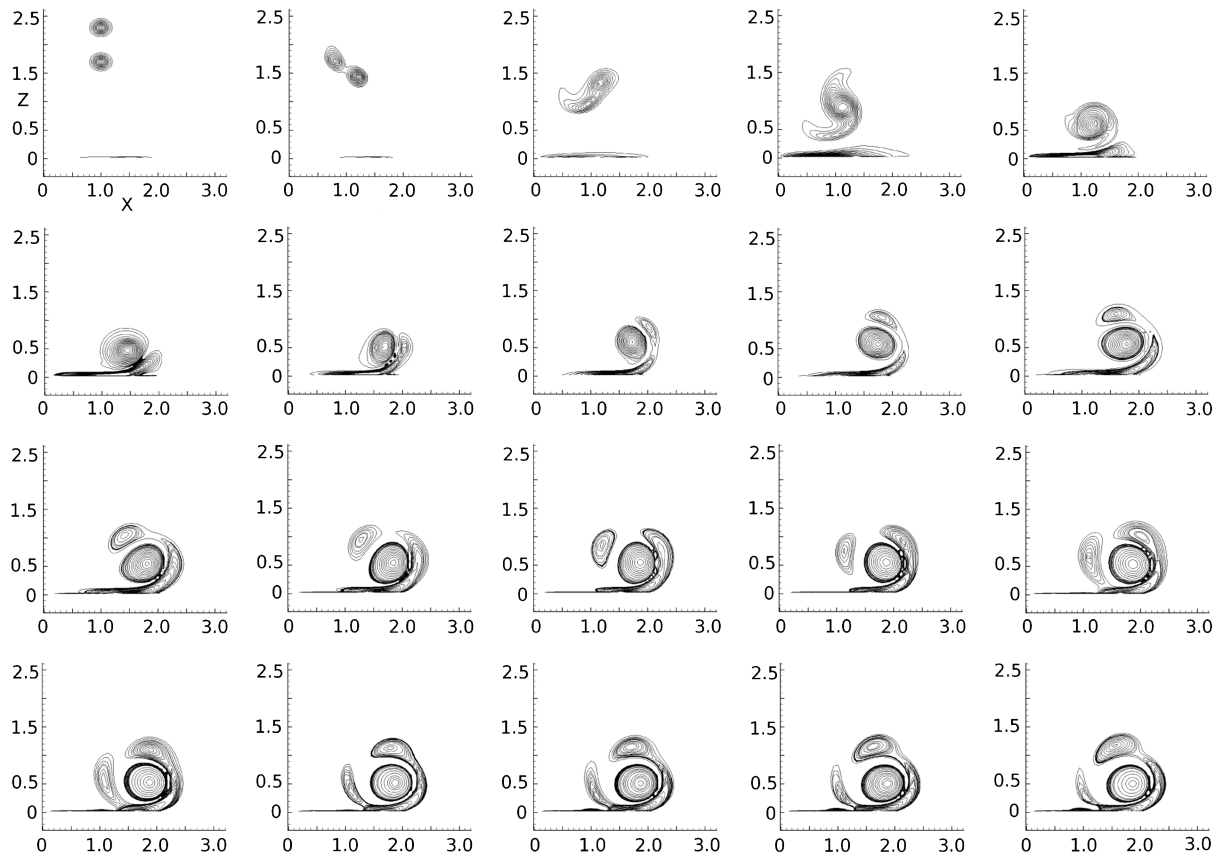Fig. 12   Vortex ring impingement on wall at Reynolds number of 1250.

Fig. 13   Two-ring impingement on wall at Reynolds number of 564 for initial separation of 0.6R; time evolution is from left to right and top to bottom.

Fig. 14   Two-ring impingement on wall at Reynolds number of 564 for initial separation of 1.0R; time evolution is from left to right and top to bottom.

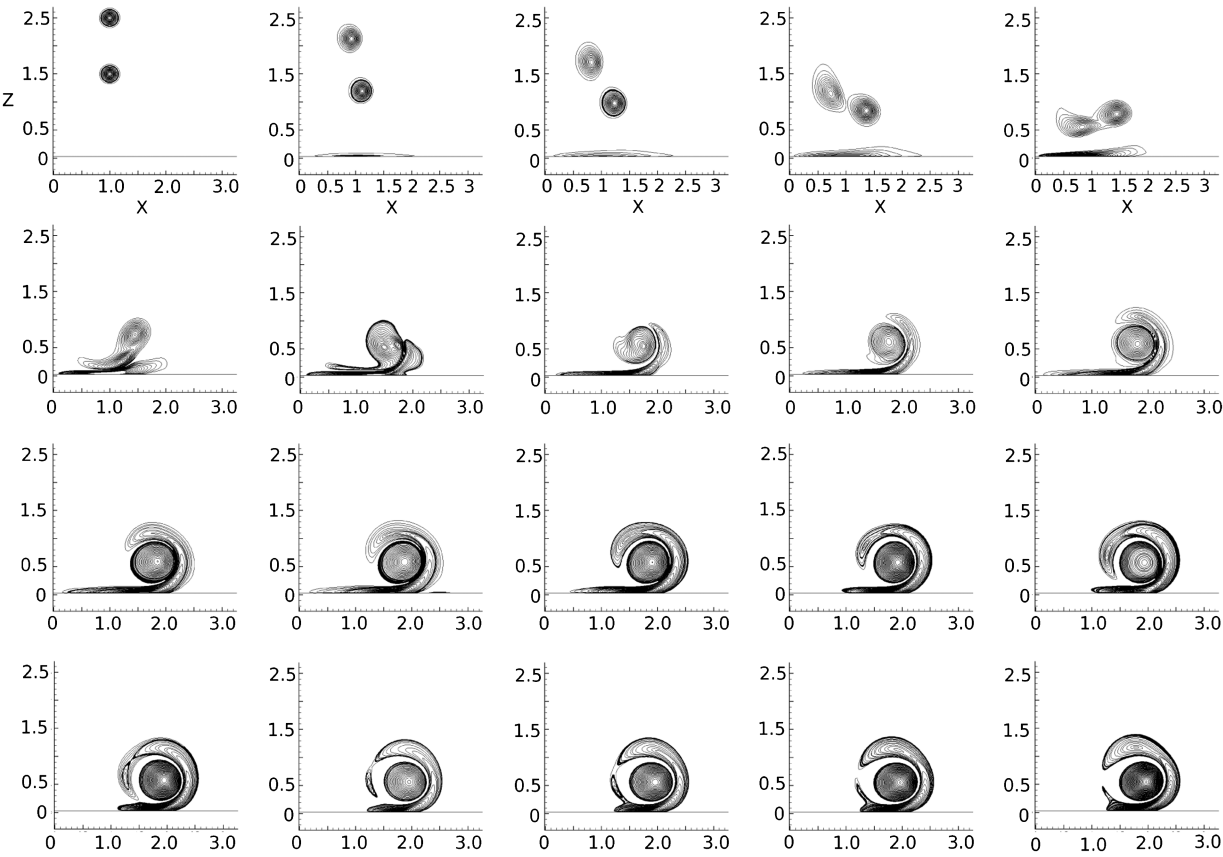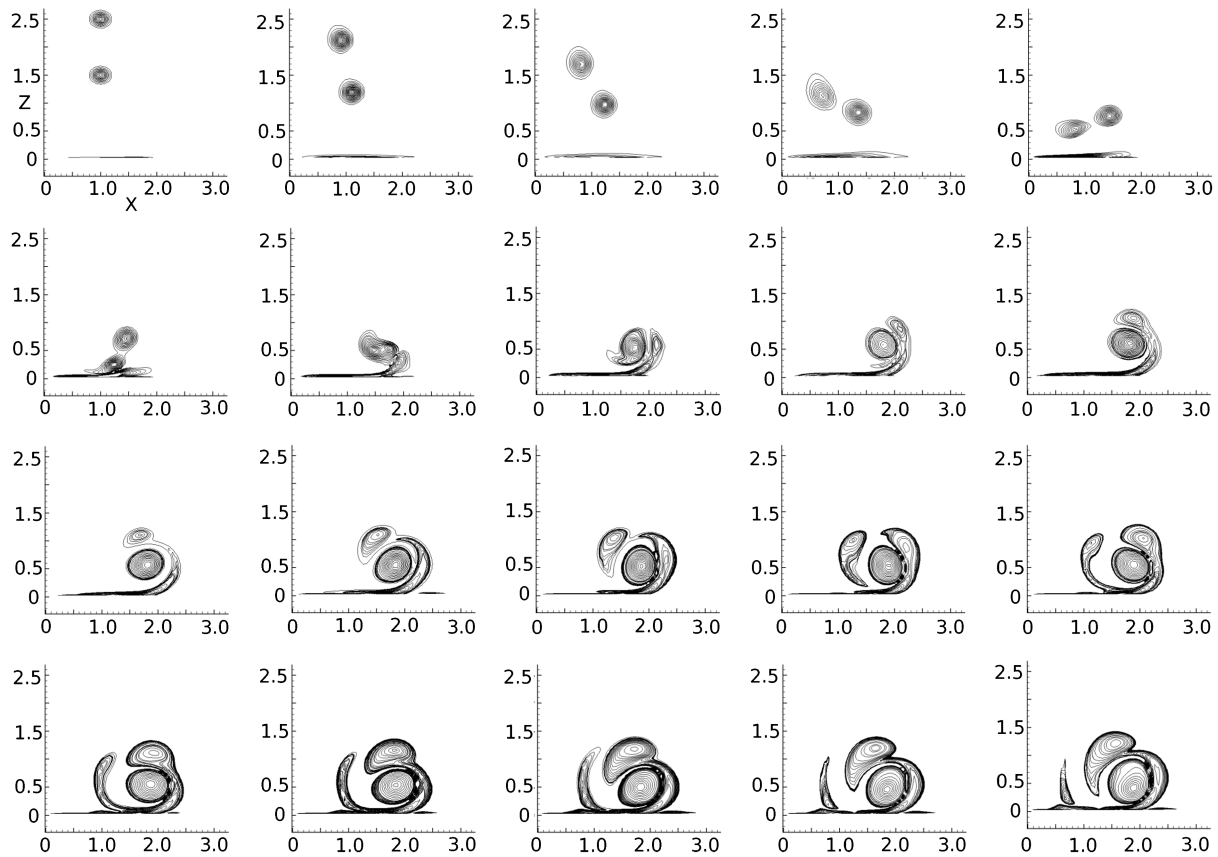**Fig. 15   Two-ring impingement on wall at Reynolds number of 1250 for initial separation of 1.0R; time evolution is from left to right and top to bottom.**

evolution of two vortex rings initially separated by a distance of $0.6R$ at a circulation-based Reynolds number of 564. The vorticity magnitude contours are plotted for an azimuthal plane. The domain is discretized using a $144 \times 144 \times 200$ clustered grid, and computations are carried out using the fifth-order WENO scheme and RK3 time stepping. No-slip boundary conditions are applied at the bottom boundary, and extrapolation boundary conditions are applied at all other boundaries. It is observed in this case that the two rings merge into a single ring before the impingement, and the flow behavior after the impingement is similar to that of an isolated ring. However, the two primary rings coalesce to form a single ring that induces a stronger counter-rotating secondary vortex in the boundary layer, compared to the case of an isolated ring at the same Reynolds number. The impingement of a single ring at this Reynolds number causes the boundary layer to wrap around the primary ring, but the interaction is not strong enough to eject a secondary ring. The impingement of two rings causes the ejection of a secondary ring and

a tertiary ring. The velocity field of the coalesced primary ring causes the secondary ring to revolve around it and rejoin the boundary layer.

Figure 14 shows the evolution of the rings for an initial separation of $1.0R$. The computations are carried out on a $300 \times 300 \times 200$ grid. The larger initial separation allows for a more pronounced leap-frogging, and the vortex rings do not coalesce before their impingement on the wall. It is observed that the velocity field of the initially leading ring pushes the initially trailing ring deeper into the boundary layer, while the velocity field of the latter pushes the former away from the wall. The two rings are observed to coalesce after the impingement of the initially trailing ring on the boundary layer. Overall, a weaker interaction is observed between the rings and the boundary layer, and no secondary or tertiary rings are ejected. This can be explained by noting that the vorticity in the boundary layer has an opposite sense of circulation, and the collision of one of the primary ring with the surface vorticity results in the weakening of both. The problem is studied for the same initial separation and at a
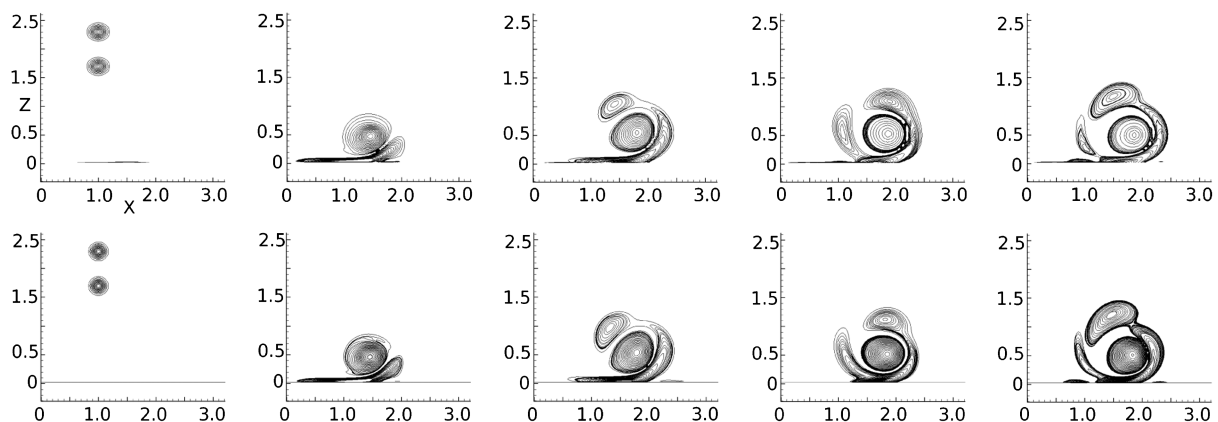

Fig. 16   Comparison of solutions obtained for two different mesh sizes: 144 × 144 × 200 (top row) and 300 × 300 × 200 (bottom row); time evolution is from left to right.

higher Reynolds number of 1250, as shown in Fig. 15. Initially, a similar behavior is seen where the initially trailing ring is pushed deeper into the boundary layer while the initially leading ring is pushed away. The two primary rings merge after the impingement. At a higher Reynolds number, the interactions are stronger, resulting in the ejection of secondary and tertiary vortex rings. It is observed that, at later times, the secondary ring induced a surface vorticity of its own, which affects its trajectory. This is not as pronounced in the previous cases studied.

A grid-convergence test is carried out to test the effect of grid refinement on the solution. Figure 16 shows the solution for the evolution of two rings at a Reynolds number of 564 with an initial separation of $0.6R$. The top row shows the solution (corresponding to every fifth plot in Fig. 13, starting from the first) obtained on a $144 \times 144 \times 200$ grid, and the bottom row shows the same solutions obtained on a $300 \times 300 \times 200$ grid. Although the results are qualitatively similar, the fine grid solution predicts a faster motion for the secondary vortex ring. This is expected because the numerical diffusion in the coarse grid solution leads to an underprediction of the velocity field of the primary ring.

B. Interactions of Multiple Rings with a Wall

The impingement of multiple vortex rings on a solid wall is studied. The flow consists of an infinite train of vortex rings approaching the wall. Although the separation between rings and the Reynolds number are expected to affect the mutual interaction between rings, the trajectories of the secondary and tertiary vortices

ejected from the boundary layer are expected to be affected by the incoming vortex rings. In the present study, an infinite train of incoming vortex rings is realized by initializing the flow to a single ring at a given initial height above the wall and adding vortex rings to the solution at periodic intervals. The ring thickness a is $0.1R$, and an initial height of $2R$ is taken.

Figure 17 shows the evolution of the problem at a Reynolds number of 1250 for an initial separation between rings of $1.0R$. A new vortex ring is introduced every third subfigure, starting with the first. As the solution progresses, the velocity fields of the vortices near the wall affect the velocities of the incoming rings, and the distance between the rings changes. However, an initial height of $2R$ ensures that the initial convection of the new vortex ring is unaffected by the previous vortices and their wall interactions. It is observed that the trajectories of the vortices right after injection are similar as the solution progresses, thus verifying this assumption. The flow is solved on a $300 \times 300 \times 200$ grid using the fifth-order WENO scheme and third-order RK time stepping. Initially, the flow is similar to that of the impingement of two rings on a wall, but it changes with the introduction of the third and subsequent rings. It is observed that, whereas the earlier primary rings coalesce near the wall, the velocity fields of the incoming rings force the coalesced structure away from the wall, thus reducing its influence on the boundary layer. The ejection of secondary vortices from the boundary layer is primarily caused by the incoming rings. The velocity field of the coalesced structure pushes the incoming rings toward the wall, as was observed in the impingement of two rings. It is also observed that the trajectories of the secondary rings are not entirely determined by the
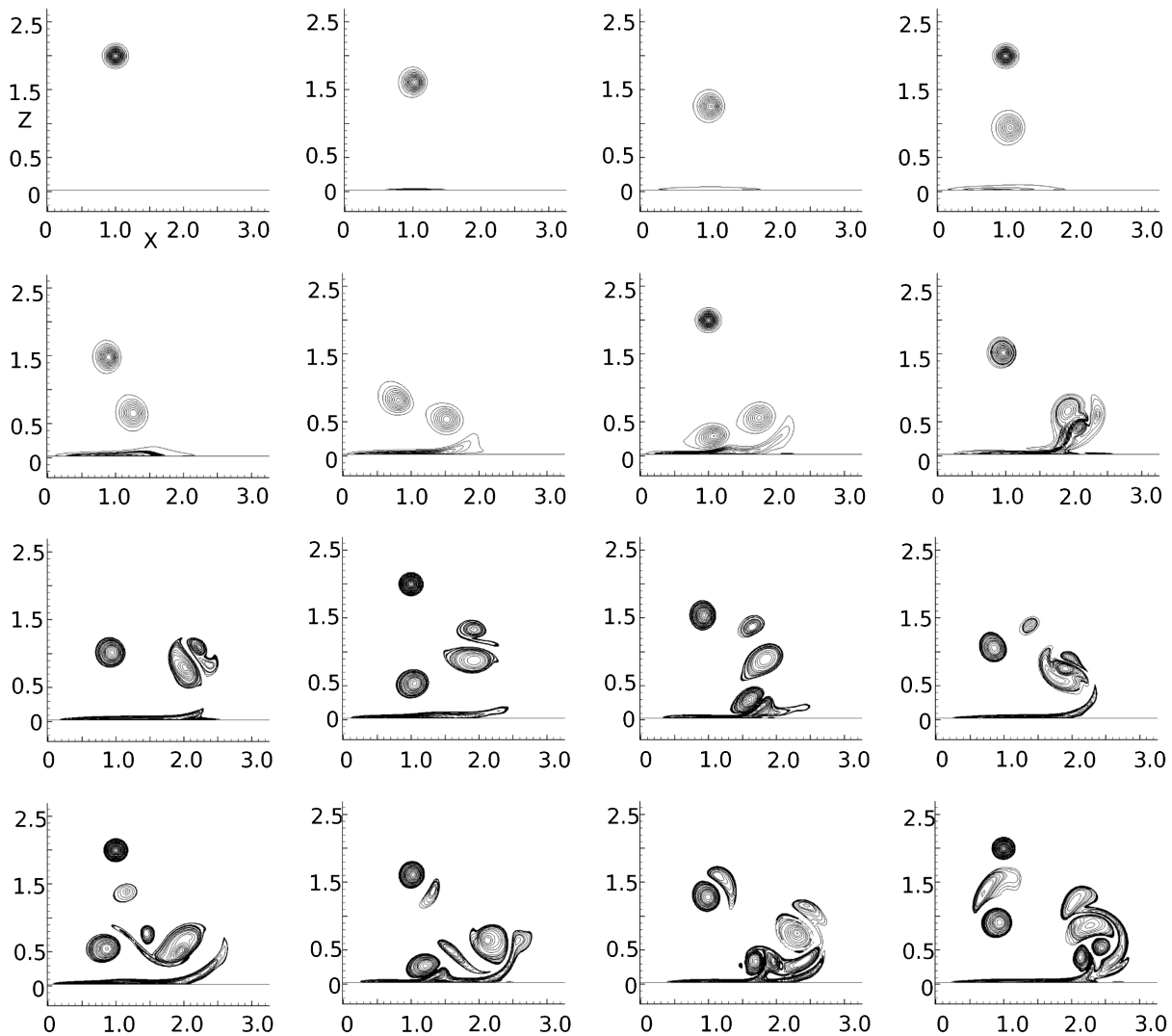

Fig. 17   Multiple-ring impingement at Reynolds number of 1250 and initial separation of 1.0R; time evolution is from left to right and top to bottom.
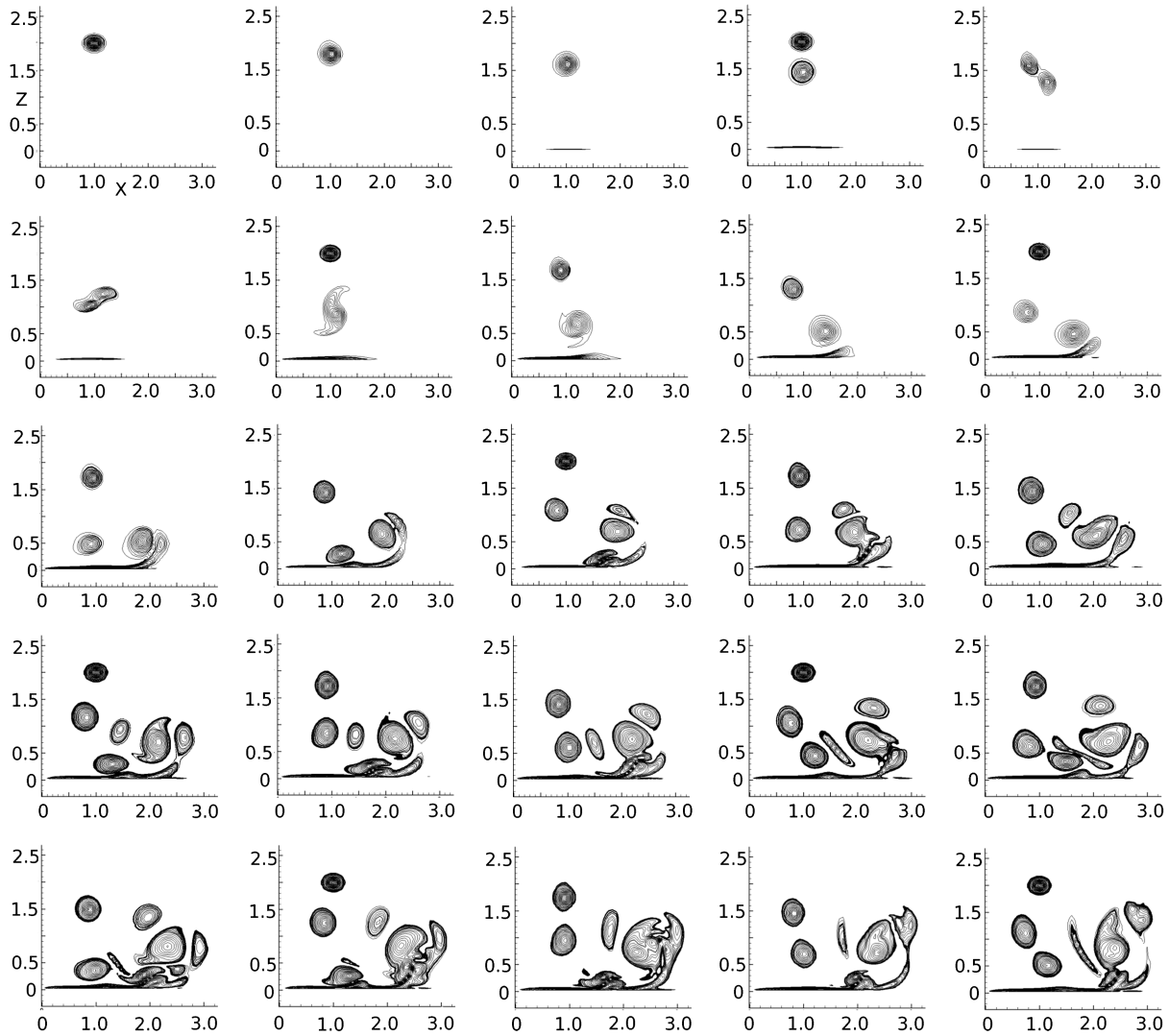
Fig. 18   Multiple-ring impingement at Reynolds number of 1250 and initial separation of 0.5R; time evolution is from left to right and top to bottom.

primary ring that caused their ejection. The secondary vortex is expected to circle around the primary vortex due to the velocity field of the latter, but an incoming vortex can cause it to break off from its previous trajectory and circle the incoming vortex. Near the wall, the flow is composed of several vortices interacting with each other. Although diffusion causes the vortices to coalesce and form larger structures, the opposing velocity fields from nearby vortices can cause a distortion of the core for smaller vortices and eventual breaking apart to form two vortices. Figure 18 shows the flow for an initial separation between the rings of $0.5R$, and it is observed that the aforementioned interactions are much more pronounced.

V.   Conclusions

A high-order algorithm is developed for the incompressible Navier–Stokes equations in the primitive variable form to study vortex-dominated flows. The governing equations are solved on a staggered Cartesian grid using the fractional-step algorithm. The algorithm uses a conservative, upwind flux reconstruction for the convective flux to yield nonoscillatory results for high-Reynolds-number flows with sharp gradients. The viscous terms are discretized using second-order central differences. The convective terms are marched in time using the second-order Adams–Bashforth or third-order Runge–Kutta schemes, while the implicit trapezoidal scheme is used for the viscous terms. The algorithm is verified for benchmark incompressible flow problems as well as problems involving vortex-dominated flows. The one-dimensional convection of an isolated vortex is studied to analyze the performance of numerical schemes

and flux formulations. Results from the upwind, conservative flux reconstruction proposed in the present study are compared with those from the nonconservative flux reconstruction. The nonconservative flux formulation is observed to yield solutions with less dissipation, while the conservative flux reconstruction is observed to model the convection speed more accurately. The upwind spatial reconstruction is shown to yield nonoscillatory solutions for inviscid problems involving strong gradients and concentrated vorticity. The algorithm is used to simulate flows involving the mutual interaction and wall impingement of vortices, and results are compared with those in literature. The viscous interaction of coplanar vortex rings and the inviscid leapfrogging of coaxial vortex rings are simulated, and the results are observed to be consistent with previous results and theoretical predictions. The two-dimensional case of a vortex dipole rebounding from a wall and the impingement of a three-dimensional vortex ring are studied, and the results agree with previous experimental/computational ones.

The algorithm is used to study the impingement of two coaxial, corotating rings on a wall. The initial separation and the Reynolds number determine the behavior of the rings before their impingement. It is seen that, for small separation and/or low Reynolds number, the rings coalesce to form a single ring before their impingement. In such a case, the behavior is qualitatively similar to that of an isolated ring, but the interactions are stronger at the same Reynolds number. At higher Reynolds number and/or larger initial separation, the rings leapfrog while approaching the wall, which results in the initially leading ring pushing the initially trailing ring further into the boundary layer while getting pushed out itself. The stronger collision

of one of the primary vortices with the counter-rotating boundary-layer vortex results in mutual weakening, and the subsequent interactions between the primary vortices and the boundary layer are weaker. The viscous interaction of multiple rings is simulated for two different initial separations. In both of these cases, it is observed that the incoming vortices push the primary vortices near the wall further out while they themselves are pushed closer to the boundary layer due to the preceding primary vortices. The incoming vortices are also observed to affect the trajectories of the secondary vortices, whose motion is otherwise determined by the primary vortex that caused their ejection. It is also observed that, while diffusion causes vortices to merge, opposing velocity fields from nearby vortices can cause core distortion and tearing of secondary vortices.

The flow simulated in the present study differs from the flow in a rotorcraft wake in two important respects. The vortices in the rotorcraft wake are helical filaments, whereas the present study deals with axis-symmetric vortex rings. The wake of a rotorcraft has a strong downwash, which dominates the convection of the vortices. In the present study, the convection of vortices are self-induced or due to mutual interactions. However, the results provide an insight in the interactions of vortices, especially near solid walls, which would be useful in understanding the wake flow for a rotorcraft operating in ground effect.

References

[1] Shariff, K., and Leonard, A., "Vortex Rings," *Annual Review of Fluid Mechanics*, Vol. 24, Jan. 1992, pp. 235–279.
doi:10.1146/annurev.fl.24.010192.001315

[2] Cerra, A. W., and Smith, C. R., "Experimental Ebservations of Vortex Ring Interaction with the Fluid Adjacent to a Surface," Lehigh Univ. Rept. FM-4, Bethlehem, PA, 1983.

[3] Verzicco, R., and Orlandi, P., "Wall/Vortex-Ring Interactions," *Applied Mechanics Reviews*, Vol. 49, No. 10, 1996, pp. 447–462.
doi:10.1115/1.3101985

[4] Sommerfield, A., *Mechanics of Deformable Bodies*, Vol. 2, Lectures of Theoretical Physics, Academic Press, New York, 1950, pp. 161–167.

[5] Riley, N., and Stevens, D. P., "A Note on Leapfrogging Vortex Rings," *Fluid Dynamics Research*, Vol. 11, No. 5, 1993, pp. 235–244.
doi:10.1016/0169-5983(93)90114-P

[6] Lim, T. T., "A Note on the Leapfrogging Between Two Coaxial Vortex Rings at Low Reynolds Numbers," *Physics of Fluids*, Vol. 9, No. 1, 1997, pp. 239–241.
doi:10.1063/1.869160

[7] Walker, J. D. A., Smith, C. R., Cerra, A. W., and Doligalski, T. L., "The Impact of a Vortex Ring on a Wall," *Journal of Fluid Mechanics*, Vol. 181, Sept. 1987, pp. 99–140.
doi:10.1017/S0022112087002027

[8] Magarvey, R. H., and MacLatchy, C. S., "The Formation and Structure of Vortex Rings," *Canadian Journal of Physics*, Vol. 42, No. 4, 1964, pp. 678–689.
doi:10.1139/p64-063

[9] Boldes, U., and Ferreri, J. C., "Behavior of Vortex Rings in the Vicinity of a Wall," *Physics of Fluids A*, Vol. 16, No. 11, 1973, pp. 2005–2006.
doi:10.1063/1.1694246

[10] Yamada, H., Hochizuki, O., Yamabe, H., and Matsui, T., "Pressure Variation on a Flat Induced by an Approaching Vortex Ring," *Journal of the Physical Society of Japan*, Vol. 54, 1985, pp. 4151–4160.
doi:10.1143/JPSJ.54.4151

[11] Liu, C. H., "Vortex Simulation of Unsteady Shear Flow Induced by a Vortex Ring," *Computers and Fluids*, Vol. 31, No. 2, 2002, pp. 183–207.
doi:10.1016/S0045-7930(01)00018-4

[12] Orlandi, P., and Verzicco, R., "Vortex Impinging on Walls: Axissymmetric and Three-Dimensional Simulations," *Journal of Fluid Mechanics*, Vol. 256, Nov. 1993, pp. 615–646.
doi:10.1017/S0022112093002903

[13] Quartapelle, L., *Numerical Solutions of the Incompressible Navier–Stokes Equations*, Vol. 113, International Series of Numerical Mathematics, Birkhauser–Verlag, Basel, Switzerland, 1993, pp. 1–175.

[14] Rempfer, D., "On Boundary Conditions for Incompressible Navier–Stokes Problems," *Applied Mechanics Reviews*, Vol. 59, No. 3, 2006, pp. 107–125.
doi:10.1115/1.2177683

[15] Ferziger, J. H., and Perric, M., *Computational Methods for Fluid Dynamics*, 3rd ed., Springer, New York, 2002, pp. 149–170.

[16] Chorin, A. J., "A Numerical Method for Solving Incompressible Viscous Flow Problems," *Journal of Computational Physics*, Vol. 2, No. 1, 1967, pp. 12–26.
doi:10.1016/0021-9991(67)90037-X

[17] Steger, J. L., and Kutler, P., "Implicit Finite-Difference Procedures for the Computation of Vortex Wakes," *AIAA Journal*, Vol. 15, No. 4, 1977, pp. 581–590.
doi:10.2514/3.60663

[18] Chorin, A. J., "Numerical Solution of the Navier–Stokes Equations," *Mathematics of Computation*, Vol. 22, No. 104, 1968, pp. 745–762.
doi:10.1090/S0025-5718-1968-0242392-2

[19] Chorin, A. J., "On the Convergence of Discrete Approximation to the Navier–Stokes Equations," *Mathematics of Computation*, Vol. 23, No. 106, 1969, pp. 341–353.
doi:10.1090/S0025-5718-1969-0242393-5

[20] Kim, J., and Moin, P., "Application of a Fractional Step Method to Incompressible Navier–Stokes Equations," *Journal of Computational Physics*, Vol. 59, No. 2, 1985, pp. 308–323.
doi:10.1016/0021-9991(85)90148-2

[21] Zhang, J., and Jackson, T. L., "A High-Order Incompressible Flow Solver with WENO," *Journal of Computational Physics*, Vol. 228, No. 7, 2009, pp. 2426–2442.
doi:10.1016/j.jcp.2008.12.009

[22] Ghia, U., Ghia, K. N., and Shin, C. T., "High-*Re* Solutions for Incompressible Flow Using the Navier–Stokes Equations and a Multigrid Method," *Journal of Computational Physics*, Vol. 48, No. 3, 1982, pp. 387–411.
doi:10.1016/0021-9991(82)90058-4

[23] Levy, D., "A Stable Semi-Discreet Central Scheme for the Two-Dimensional Incompressible Euler Equations," *IMA Journal of Numerical Analysis*, Vol. 25, No. 3, 2005, pp. 507–522.
doi:10.1093/imanum/dri004

[24] Kida, S., Takaoka, M., and Hussain, F., "Collision of Two Vortex Rings," *Journal of Fluid Mechanics*, Vol. 230, Sept. 1991, pp. 583–646.
doi:10.1017/S0022112091000903

[25] Hahn, S., and Iaccarino, G., "Towards Adaptive Vorticity Confinement," *47th AIAA Aerospace Sciences Meeting*, Orlando, FL, AIAA Paper 2009-1613, Jan. 2009.

[26] Orlandi, P., "Vortex Dipole Rebound from a Wall," *Physics of Fluids A*, Vol. 2, No. 8, 1990, pp. 1429–1436.
doi:10.1063/1.857591

[27] Jiang, G. S., and Shu, C. W., "Efficient Implementation of Weighted ENO Schemes," *Journal of Computational Physics*, Vol. 126, No. 1, 1996, pp. 202–228.
doi:10.1006/jcph.1996.0130

[28] Zedan, M., and Scheider, G. E., "A Three-Dimensional Modified Strongly Implicit Procedure for Heat Conduction," *AIAA Journal*, Vol. 21, No. 2, 1983, pp. 295–303.
doi:10.2514/3.8068

G. Blaisdell
Associate Editor